G331.512-0.103: AN INTERSTELLAR LABORATORY FOR MOLECULAR SYNTHESIS
I THE ORTHO-TO-PARA RATIOS FOR CH$_3$OH AND CH$_3$CN

Edgar Mendoza,[1] Leonardo Bronfman,[2] Nicolas U. Duronea,[3] Jacques R. D. Lépine,[1] Ricardo Finger,[2]
Manuel Merello,[4] Carlos Hervías-Caimapo,[2,5] Diana R. G. Gama,[1] Nicolas Reyes,[6] and Lars Åke-Nyman[7]

[1] *Universidade de São Paulo, IAG Rua do Matão, 1226, Cidade Universitária, 05508-090, São Paulo, Brazil*

[2] *Departamento de Astronomía, Universidad de Chile, Casilla 36-D, Santiago de Chile, Chile*

[3] *Instituto Argentino de Radioastronomía, IAR CONICET, CCT-La Plata, C.C.5., 1894, Villa Elisa, Argentina*

[4] *Istituto di Astrofisica e Planetologia Spaziali-INAF Via Fosso del Cavaliere 100, I-00133 Roma, Italy*

[5] *Jodrell Bank Centre for Astrophysics, School of Physics and Astronomy, University of Manchester, Oxford Road, Manchester M139PL, UK*

[6] *Electrical Engineering Department, Universidad de Chile, Av. Tupper 2007, Santiago, Chile*

[7] *Joint ALMA Observatory, JAO Alonso de Córdova 31070, Vitacura, Santiago de Chile, Chile*

ABSTRACT

Spectral line surveys reveal rich molecular reservoirs in G331.512-0.103, a compact radio source in the center of an energetic molecular outflow. In this first work, we analyse the physical conditions of the source by means of CH$_3$OH and CH$_3$CN.

The observations were performed with the APEX telescope. Six different system configurations were defined to cover most of the band within (292–356) GHz; as a consequence we detected a forest of lines towards the central core.

A total of 70 lines of A/E-CH$_3$OH and A/E-CH$_3$CN were analysed, including torsionally excited transitions of CH$_3$OH (ν_t=1). In a search for all the isotopologues, we identified transitions of ^{13}CH$_3$OH. The physical conditions were derived considering collisional and radiative processes. We found common temperatures for each A and E symmetry of CH$_3$OH and CH$_3$CN; the derived column densities indicate an A/E equilibrated ratio for both tracers. The results reveal that CH$_3$CN and CH$_3$OH trace a hot and cold component with $T_k \sim 141$ K and $T_k \sim 74$ K, respectively. In agreement with previous ALMA observations, the models show that the emission region is compact ($\lesssim 5.5''$) with gas density $n(\mathrm{H_2})$=(0.7–1) $\times 10^7$ cm^{-3}. The CH$_3$OH/CH$_3$CN abundance ratio and the evidences for pre-biotic and complex organic molecules suggest a rich and active chemistry towards G331.512-0.103.

Keywords: ISM: molecules – Molecular processes – Radio lines: ISM

Corresponding author: Edgar Mendoza
emendoza@usp.br

1. INTRODUCTION

G331.512-0.103 is one of the most luminous and energetic molecular outflows known in the Galaxy. All the system is embedded in a star forming region known as G331.5-0.1, located in the Norma spiral arm at a distance of $\sim$ 7 pc. This source exhibits typical H II region properties and intense maser emission of OH and CH_3OH (Caswell 1998; Nyman et al. 2001; Bronfman et al. 2008). At the center of the system, a young and massive stellar object drives a bipolar flow of around $55 M_\odot$ with a momentum of $\sim$ 2.4 $\times$ 10^3 $M_\odot$ km s^{-1}. Radio continuum observations have revealed a compact and central structure associated to a dust core. The central region has been also mapped with ALMA observations with transitions of SiO (8–7), $H^{13}CO^+$ (4–3), HCO^+ (4–3) and CO (3–2). The observations revealed a ring-like structure, consistent with a cavity, and the existence of a high velocity outflow emission confined in a region lower than 5″ in size (Merello et al. 2013a,b; Hervías et al. 2015). In this work, we present new results on the emission of CH_3OH and CH_3CN detected towards the central core, denominated hereafter as G331.

As an interstellar laboratory, G331 exhibits active chemistry in pre-biotic and complex organic molecules likely stimulated by physical processes in the molecular core and outflow. With the Atacama Pathfinder EXperiment APEX telescope, we have detected a vast number of molecular lines potentially linked to reservoirs traced by CH_3OH and CH_3CN. Those tracers are excellent candidates to unveil the different physical components that O- and N-bearing molecules can reveal towards hot molecular cores (Sandell et al. 1994; Wyrowski et al. 1999; Jørgensen et al. 2004; Beuther et al. 2005; Fontani et al. 2007; Fuente et al. 2014; Giannetti et al. 2017). In addition, from a chemical point of view, CH_3OH and CH_3CN are considered as parent and daughter molecules, respectively, in the route of interstellar molecular formation (e.g. Nomura & Millar 2004). With that motivation, we started a systematic study of G331 beginning with spectral analyses of A/E-CH_3OH and A/E-CH_3CN.

1.1. *The tracers CH_3CN and CH_3OH*

CH_3CN (methyl cyanide) is a symmetric top molecule. The nuclear spin state of the hydrogen atoms defines whether the molecule has an ortho (E) or para (A) symmetry. Rotational levels of CH_3CN are characterized by two quantum numbers: the total angular momentum (J) and its projection on the axis of symmetry (K). Spectral signatures are associated to K-ladder structures whose notation for the A and E configurations are $K = 3n$ and $K = 3n\pm1$, respectively (Solomon et al. 1971; Boucher et al. 1980; Cummins et al. 1983).

CH_3OH (methanol) is one of the simplest asymmetric-top molecules, however its spectrum is quite complicated since there is a strong coupling between torsional and vibrational modes. Methanol also exists in two species denoted as A and E depending on the nuclear spin alignment of the three H-atoms of the methyl group (CH_3). The energy levels of methanol can be assigned with the total angular momentum J and its component K along the symmetry axis (Lees & Baker 1968; Lovas et al. 1982).

The excellent spectral resolution of the used instrument allowed us to study separately the A and E isomers of CH_3CN and CH_3OH. Nuclear spin conversion of A and E symmetries are considered as rare events, being affected by chemical reactions, non-reactive collisions and grain-surface mechanisms (Willacy et al. 1993; Hugo et al. 2009). However, the spin conversion has a particular relevance in molecular astrophysics. Important questions remain unsolved, for instance, how collisions stimulate conversions and, as a consequence, if that property can be used as an astronomical clock (Lee et al. 2006; Sun et al. 2015). One of our goals is to verify if the A and E pairs are equally populated at the local temperature of the source (e.g Andersson et al. 1984; Minh et al. 1993; Wirström et al. 2011).

We organized this paper as follows: in section 2 the observational procedure is described. In section 3 results about the line identification are presented. In section 4 we discuss the radiative analysis. The discussion, conclusions and perspectives are presented in sections 5 and 6.

2. OBSERVATIONS AND METHODOLOGY

The observations were carried out in March 2016 with the Atacama Pathfinder Experiment Telescope (APEX), located at *Llano de Chajnantor* (Chilean Andes). The spectra were obtained using the single point mode towards the coordinates RA, Dec.(J2000) = $16^h 12^m 10.1^s$, $-51°28'38.1''$. We used the APEX-2 receiver of the Swedish Heterodyne Facility Instrument (SHeFI) as frontend (Güsten et al. 2006; Risacher et al. 2006). The employed backend was the eXtended bandwidth Fast Fourier Transform Spectrometer2 (XFFTS2), which consists of two units with a bandwidth of 2.5 GHz divided into 32768 channels. We selected six set-ups to cover a band ranging from 292 GHz to 356 GHz; they are summarized in Table 1. The integration time was estimated to obtain a conservative rms noise of $\sim$ 25 mK; then each set-up expended integration times between 0.7 and 2.6 hs, with system temperatures in the range of $T_{sys} \sim$(200–380) K.

The calibration was done applying the chopper-wheel technique. The output intensity provided by the system was obtained in a scale of T_A^*, which represents the antenna temperature corrected by atmospheric attenuation. The observed intensities were converted to the main-beam temperature scale using $\eta_{mb} = 0.73$, the main beam efficiency for APEX-2 (Güsten et al. 2006).

All the K-ladders structures appeared closely spaced in a wide range of frequencies, so that they were ob-

Table 1. List of set-ups observed with the APEX-2 SHeFI instrument towards G331.

Set-up centred at	Frequency (GHz)	Beam ($''$)	Resolution (10^{-2} km s^{-1})
CH$_3$CN (16–15)	292 – 296	21.4	7.7
CH$_3$CN (19–18)	329 – 333	19.0	6.9
CH$_3$OH (7–6)	336 – 340	18.6	6.8
SO (8–7)	343 – 347	18.2	6.6
CH$_3$OCH$_3$ (11–10)	347 – 351	17.9	6.5
HCOOCH$_3$ (33–32)	352 – 356	17.7	6.4

served with the same receiver. This fact helped us with the inspection of irregularities due to calibration uncertainties, for which we adopted an error of 20 %.

The data reduction was carried out with the CLASS package of the GILDAS software.[1] The line identification was performed using the NIST[2] (Lovas et al. 2009), CDMS[3] (Müller et al. 2005) and JPL[4] (Pickett et al. 1998) spectroscopy databases. Specifically, the CDMS and JPL catalogues were interactively loaded on the survey using the Weeds extension of CLASS. The radiative analyses were performed using the CASSIS software.[5]

3. RESULTS

3.1. *A/E-CH$_3$CN*

We observed the transitions CH$_3$CN J=16–15, J=18–17 and J=19–18; a set of them is displayed in Figure 1. Within those levels, the spectral resolution was high enough to separate the components K=0, 3, 6 and 9 from K=1, 2, 4, 5, 7 and 8, which correspond to A-CH$_3$CN and E-CH$_3$CN, respectively (see Table 2).

The line identification was performed overlapping the laboratory values on the observed spectral bands at the rest velocity of the source. A high coincidence was obtained, since the K-ladder structures appeared separately and well centred, at the source's rest frequency (with V_{lsr}=-90 km s^{-1}), as predicted by the spectroscopic databases (Figure 1). This inspection revealed that most of the lines have a Gaussian profile, but only few of them presented broad blue and red wings due to the outflow activity. We applied Gaussian functions to fit and model the emission. For that, the spectral line processing was carried out using the CLASS package, by means of which we fitted baselines and Gaussian functions for each processed line. As a result, we have

listed in Table 2 the Gaussian fit parameters and uncertainties of each analysed line; those parameters are the integrated line flux ($\int T_{mb}dV$ in K km s^{-1}), local standard of rest (LSR) velocity (V_{lsr} in km s^{-1}) and the line width given by the full width at half maximum (FWHM in km s^{-1}).

From a simple comparison of the A-CH$_3$CN fluxes, we observed a stiff increase of them as the lines go from the K=6 to K=0 transitions. This behaviour is in agreement with the probabilities predicted by the Einstein coefficients (A_{ij}). For the transitions with J_{up}=16, 18 and 19, the obtained patterns are 16_6:16_3:$16_0 \approx$ 1:3:4, 18_6:18_3:$18_0 \approx$ 1:4:6 and 19_6:19_3:$19_0 \approx$ 1:1:2, respectively. Only few transitions diverged from this pattern, namely, A-CH$_3$CN J=18_6–17_6 and J=19_3–18_3, whose emission appeared blended with HNCO ($15_{1,14}$-$14_{1,13}$) and C$_2$H ($4_{4,4} - 3_{3,2}$) at 330848 MHz and 349400 MHz, respectively. Those contaminant transitions were previously detected by Jewell et al. (1989) and Sutton et al. (1991) in Orion A and OMC-1.

For $E-$CH$_3$CN lines, the derived fluxes also increase when the K-ladders vary from 7 to 1. That is in agreement with the spontaneous decay rates predicted by Aij. For the transitions with J_{up}=16, 18 and 19, the complete patterns are 16_7:16_5:16_4:16_2:$16_1 \approx$ 1:2:3:5:10, 18_7:18_5:18_4:18_2:$18_1 \approx$ 1:3:4:8:12 and 19_7:19_5:19_4:19_2:$19_1 \approx$ 1:7:7:12:26, respectively. Here the transition E-CH$_3$CN J=19_4–18_4 at 349346 MHz appeared blended with C$_2$H ($4_{5,4} - 3_{4,3}$) at 349339 MHz. We also found that the transition E-CH$_3$CN J=$19_7 - 18_7$ at 349125 MHz might be blended with CH$_3$OCHO at 349124 MHz.

The search for the high levels K=8 and K=9 yielded negative results, we did not detect lines of these K-ladder numbers above the detection limit of the APEX data. For the cases A-CH$_3$CN (16_9-15_9) and (19_9-18_9), we did not observe emission at all. In the case of the 18_9-17_9 line, we obtained a marginal flux from the Gaussian fits. This line also might be blended with c-C$_3$HD and/or *weeds*,[6] see Table 2. For the cases E-CH$_3$CN (16_8-15_8) and (18_8-17_8), the emission appeared fully and partially blended with CS (6–5) and ^{34}SO$_2$ (21_2-21_1), respectively. For the 19_8-18_8 transition, we did not detect emission. The results are listed in Table 2. In addition, a search for emission of CH$_3$CN ($v_8 = 1$) was performed with the current dataset; however we did not observe clear evidences to conclude about its presence in G331.

3.2. *A/E-CH$_3$OH*

As a forest of spectral lines (Figure 1), the main part of the CH$_3$OH emission has appeared only in an interval of 3 GHz along the whole survey. The lines were identified
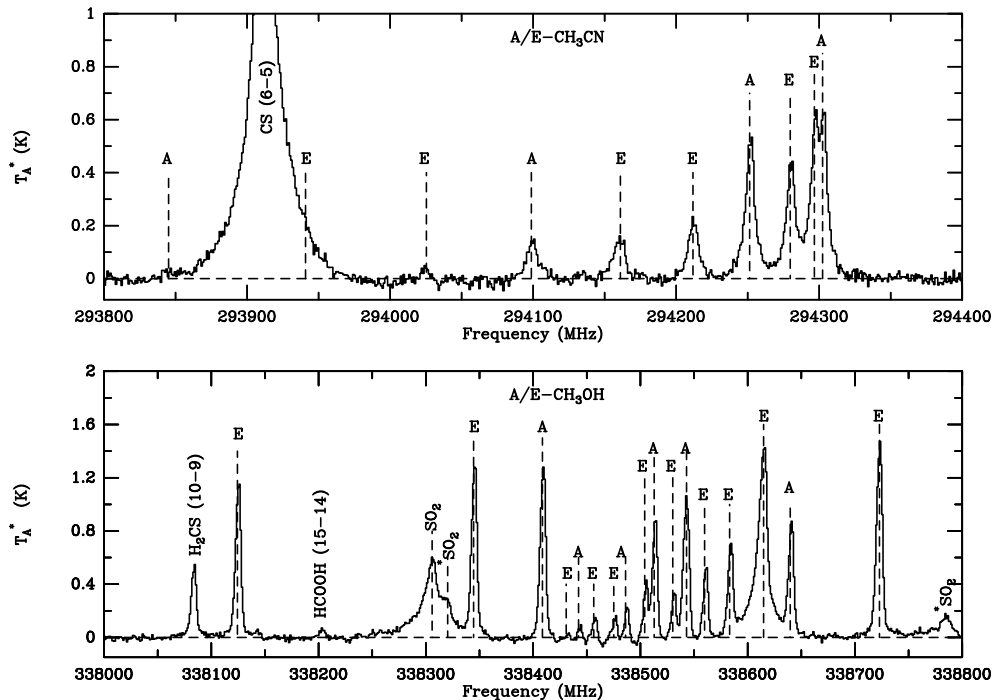
Figure 1. Lines of A/E-CH$_3$CN and A/E-CH$_3$OH as observed with the APEX-2 SHeFI instrument towards G331. Lines were adjusted to their rest frequencies using the CDMS and JPL catalogues. Due to the high intensity of the methanol lines, the range of the y-axis is different in both panels.

by a simple comparison of their frequencies, corrected by the source V_{lsr}=-90 km s^{-1}, with the rest frequencies reported in molecular databases. The methanol lines exhibit a symmetrical distribution which were fitted by simple Gaussian functions. The spectroscopic and fit parameters estimated for these lines are listed in Table 3. We find a FWHM of around 5.5 km s^{-1} and a V_{lsr}=-90 km s^{-1} with a dispersion of $\pm$ 2km s^{-1}, mainly due to lines which exhibited a low signal-to-noise ratio. In Figure 1 we show a set of A and E-CH$_3$OH lines with J=7–6.

Although most of the methanol emission corresponds to the torsional ground state, we also identified lines corresponding to the first excited state (ν_t=1). Such is the case for the lines displayed in Figure 2 (upper panel), where it is observed a broad line of ^{34}SO at $\sim$ 337580 MHz blended with the transition E-CH$_3$OH (ν_t=1) $7_4 - 6_4$ at a frequency, corrected by the source V_{lsr}, of 337581.663 MHz. Around the ^{34}SO peak, minor satellite emission also was identified as corresponding to (A/E)-CH$_3$OH $\nu_t = 1$; the spectroscopic parameters are summarized in Table 4. In the bottom panel of Figure 2 we display the only excited line without contaminant emission, which corresponds to A-CH$_3$OH (ν_t=1) $7_1 - 6_1$ at a frequency, corrected by the source V_{lsr}, of 337969.414 MHz.

Emission of excited methanol is typically observed towards hot molecular cores. For instance, Menten et al. (1986), Sutton et al. (1995) and Schilke et al. (2001) have reported its emission in OMC-1, W3(OH) and

W51.

The observed lines of excited methanol constitute an evidence for its presence in G331. However, in order to solve questions as whether the excited emission is populated or not at the same conditions of the ground state, it is necessary to carry out complementary observations; for instance, at frequencies between 600–720 GHz. These observations could reveal a larger number of CH$_3$OH ν_t=1,2 lines favouring a better estimation on the physical conditions. In the bottom panel of Figure 2, we displayed a broad line close to 337900 MHz which is associated to SO$_2$; however, that line could be also blended with CH$_3$OH (ν_t=2) J=7–6 at 337877 MHz.

3.3. Isotopologues

We searched for lines of the D, ^{13}C, ^{15}N and ^{18}O isotopologues of CH$_3$CN and CH$_3$OH. As predicted by the spectroscopic databases, several frequencies of those isotopologues fall across the bands; however we only confirm the presence of ^{13}CH$_3$OH. Emission related to ^{13}CH$_3$CN J=19–18 was also identified; however, the lines are blended with SO J=3–2 at 339341 MHz. Those lines were also reported by Jewell et al. (1989) in Orion A.

We detected a couple of transitions of A-^{13}CH$_3$OH. The associated spectroscopic parameters are presented in Table 5. The lines were identified at the rest frequencies 330252.798 MHz and 350103.118 MHz with signal-to-noise ratios of $S/N \geq 5$. Such detections

Table 2. Spectral line analysis of A-CH$_3$CN and E-CH$_3$CN in G331. Columns 1–4 list the spectroscopic parameters collected from databases such as CDMS and JPL. Columns 5–7 contain the resulting parameters and uncertainties derived from Gaussian fits, they are line flux ($\int T_{mb}dV$), local standard of rest velocity (V_{lsr}) and the line width (FWHM).

Transition	Frequency (MHz)	E_u (K)	A_{ij} (10^{-3} s^{-1})	$\int T_{mb}dV$ (K km s^{-1})	V_{lsr} (km s^{-1})	FWHM (km s^{-1})
A-CH$_3$CN						
[†]16_9–15_9	293845.164	697.83	1.51	–	–	–
16_6–15_6	294098.867	377.0721	1.9	2.065 ± 0.006	-90.7 ± 0.2	10.3 ± 0.5
16_3–15_3	294251.461	184.3532	2.13	5.9 ± 0.3	-90.4 ± 0.2	8.2 ± 0.6
16_0–15_0	294302.388	120.0696	2.21	7.9 ± 0.2	-89.69 ± 0.07	8.8 ± 0.2
[a]18_9–17_9	330557.569	728.67	2.36	0.15 ± 0.04	-91.2 ± 0.1	0.9 ± 0.2
[b]18_6–17_6	330842.762	407.9468	2.8	1.53 ± 0.07	-88.2 ± 0.4	10 ± 0.1
18_3–17_3	331014.296	215.2437	3.07	6.6 ± 0.5	-90.3 ± 0.3	8.9 ± 0.8
18_0–17_0	331071.544	150.9654	3.16	9.1 ± 0.3	-89.5 ± 0.1	9.4 ± 0.3
[†]19_9–18_9	348911.401	745.42	2.87	–	–	–
19_6–18_6	349212.311	424.7065	3.34	3.01 ± 0.01	-90.4 ± 0.2	11.5 ± 0.5
[c]19_3–18_3	349393.297	232.012	3.63	3.66 ± 0.07	-91.7 ± 0.3	3.8 ± 0.6
19_0–18_0	349453.7	167.7368	3.72	5.5 ± 0.3	-90.5 ± 0.1	6.8 ± 0.4
E-CH$_3$CN						
[d]16_8–15_8	293940.916	568.69	1.65	–	–	–
16_7–15_7	294025.496	461.7635	1.78	0.8 ± 0.1	-88.7 ± 0.6	10 ± 2
16_5–15_5	294161.001	290.5519	1.99	2.14 ± 0.09	-89.2 ± 0.2	9.8 ± 0.5
16_4–15_4	294211.873	226.3073	2.07	2.93 ± 0.08	-90.2 ± 0.1	9.3 ± 0.3
16_2–15_2	294279.75	140.6138	2.17	4.19 ± 0.09	-90.79 ± 0.08	7.9 ± 0.2
16_1–15_1	294296.728	119.1843	2.2	7.74 ± 0.07	-91.87 ± 0.07	9.4 ± 0.1
[e]18_8–17_8	330665.206	599.54	2.52	1.21 ± 0.07	-91.4 ± 0.2	8.1 ± 0.5
18_7–17_7	330760.284	492.6304	2.67	0.8 ± 0.1	-90.8 ± 0.7	11 ± 2
18_5–17_5	330912.608	321.4329	2.91	2.9 ± 0.1	-89.4 ± 0.2	11.6 ± 0.6
18_4–17_4	330969.794	257.1937	3	3.3 ± 0.1	-90.5 ± 0.1	9.2 ± 0.4
18_2–17_2	331046.096	171.5073	3.12	6.66 ± 0.09	-90.87 ± 0.07	10.4 ± 0.2
18_1–17_1	331065.181	150.0797	3.15	10.252 ± 0.007	-91.62 ± 0.06	10.6 ± 0.1
[†]19_8–18_8	349024.971	616.29	3.05	–	–	–
[f]19_7–18_7	349125.287	509.38	3.2	0.304 ± 0.003	-90.1 ± 0.6	5.9 ± 0.7
19_5–18_5	349286.006	338.1962	3.45	2.106 ± 0.008	-89.6 ± 0.2	9.5 ± 0.5
[g]19_4–18_4	349346.343	273.9599	3.55	2.091 ± 0.002	-89.76 ± 0.09	6.1 ± 0.1
19_2–18_2	349426.85	188.2773	3.67	5.3 ± 0.1	-90.61 ± 0.9	9.8 ± 0.2
19_1–18_1	349446.987	166.8506	3.71	8.018 ± 0.001	-91.76 ± 0.05	9.39 ± 0.08

NOTE—Likely blended lines with (a) HCOOCH$_2$CH$_3$ (330557 MHz) and/or c-C$_3$HD (330558 MHz), (b) HNCO (330848 MHz), (c) C$_2$H (349400 MHz), (d) CS (293912 MHz), (e) ^{34}SO$_2$ (330667 MHz), (f) CH$_3$OCHO (349124 MHz) and (g) C$_2$H (349339 MHz). †Marginal emission ($< 5\sigma$).

have been fundamental to analyse the opacity of the detected emission. For instance, we estimated flux ratios using lines of A-^{13}CH$_3$OH and A-CH$_3$OH with comparable spectroscopy, namely, using those transitions

Table 3. The table 2 caption applies here for A-CH$_3$OH and E-CH$_3$OH.

Transition J_k	Frequency (MHz)	E_u (K)	A_{ij} (10^{-5} s^{-1})	$\int T_{mb}dV$ (K km s^{-1})	V_{lsr} (km s^{-1})	FWHM (km s^{-1})
A-CH$_3$OH						
6_1–5_1	292672.889	63.707	10.6	6.95 ± 0.06	-90.67 ± 0.02	5.24 ± 0.05
3_2–4_1	293464.055	51.6381	2.89	3.39 ± 0.09	-90.35 ± 0.09	6.8 ± 0.2
12_2–11_3	329632.881	218.8033	6	0.59 ± 0.07	-89.8 ± 0.3	4.1 ± 0.6
11_1–11_0	331502.319	169.0101	19.6	3.394 ± 0.001	-90.17 ± 0.02	2.82 ± 0.03
$^\dagger 7_3$–8_1	332920.822	114.794	1.15×10^{-5}	–	–	–
12_1–12_0	336865.149	197.0765	20.3	6.9 ± 0.5	-91.9 ± 0.2	6.9 ± 0.3
7_0–6_0	338408.698	64.9817	17	10.83 ± 0.07	-90.51 ± 0.02	5.31 ± 0.04
7_6–6_6	338442.367	258.6994	4.53	1.09 ± 0.06	-91.3 ± 0.1	5.7 ± 0.4
7_5–6_5	338486.322	202.8864	8.38	2.11 ± 0.08	-90.98 ± 0.09	4.9 ± 0.2
7_2–6_2	338512.853	102.7032	15.7	7.3 ± 0.4	-90.5 ± 0.1	5.5 ± 0.4
7_3–6_3	338543.152	114.7948	13.9	9.21 ± 0.08	-89.77 ± 0.02	5.62 ± 0.05
7_2–6_2	338639.802	102.7179	15.7	7.4 ± 0.7	-90.6 ± 0.2	5.6 ± 0.6
2_2–3_1	340141.143	44.6729	2.79	2.14 ± 0.06	-90.71 ± 0.08	5.5 ± 0.2
$^\dagger 16_1$–15_2	345903.916	332.6545	9.02	–	–	–
5_4–6_3	346204.271	115.1625	2.17	2.31 ± 0.07	-90.74 ± 0.09	5.9 ± 0.2
14_1–14_0	349106.997	260.2068	22	4.25 ± 0.06	-90.77 ± 0.04	5.41 ± 0.09
1_1–0_0	350905.1	16.841	33.1	12.19 ± 0.05	-90.58 ± 0.01	5.13 ± 0.03
$^\dagger 8_2$–9_0	351685.48	121.2915	16.2	–	–	–
$^\dagger 10_4$–11_2	355279.539	207.9929	1.22×10^{-3}	–	–	–
13_0–12_1	355602.945	211.0285	12.6	4.02 ± 0.04	-91.01 ± 0.02	4.76 ± 0.06
15_1–15_0	356007.235	295.2675	23	2.68 ± 0.05	-90.46 ± 0.05	5.8 ± 0.1
E-CH$_3$OH						
8_{-3}–9_{-2}	330793.887	138.3774	5.38	1.96 ± 0.06	-91.03 ± 0.07	4.6 ± 0.1
16_{-1}–15_{-2}	331220.371	312.7333	5.23	0.55 ± 0.06	-91.4 ± 0.3	5.3 ± 0.6
3_3–4_2	337135.853	53.7412	1.58	1.09 ± 0.06	-91.1 ± 0.1	4.7 ± 0.3
$^\dagger 7_2$–6_2	337671.238	456.8285	15.5	–	–	–
$^\dagger 7_5$–6_5	337685.248	486.0568	8.28	–	–	–
$^\dagger 7_{-1}$–6_{-1}	337707.568	470.3161	16.5	–	–	–
7_0–6_0	338124.488	70.1794	16.9	9.09 ± 0.06	-90.74 ± 0.01	5.01 ± 0.04
7_{-1}–6_{-1}	338344.588	62.6521	16.6	9.61 ± 0.08	-90.63 ± 0.02	4.87 ± 0.05
$^\dagger 7_6$–6_6	338404.61	235.8941	4.51	–	–	–
$^\dagger 7_{-6}$–6_{-6}	338430.975	246.0504	4.54	–	–	–
7_{-5}–6_{-5}	338456.536	181.1017	8.34	1.3 ± 0.4	-90.9 ± 0.7	5 ± 2
7_5–6_5	338475.226	193.1625	8.34	1.5 ± 0.6	-91 ± 0.1	5 ± 3
7_{-4}–6_{-4}	338504.065	144.9961	11.5	4 ± 2	-91.3 ± 0.04	6 ± 1
7_4–6_4	338530.257	153.0934	11.5	3.1 ± 0.6	-91.1 ± 0.4	5 ± 1
7_{-3}–6_{-3}	338559.963	119.8084	14	4.5 ± 0.1	-90.93 ± 0.6	5.2 ± 0.1
7_3–6_3	338583.216	104.8115	13.9	6.9 ± 0.2	-90.99 ± 0.08	6.6 ± 0.2
7_1–6_1	338614.936	78.1537	17.1	21.4 ± 0.8	-89.5 ± 0.2	9.9 ± 0.5
7_{-2}–6_{-2}	338722.898	83.0148	15.7	12.53 ± 0.07	-90.04 ± 0.01	5.61 ± 0.03
$^\dagger 18_2$–17_3	344109.039	411.5062	6.79	–	–	–

Note—†Marginal emission ($< 5\sigma$).

Table 4. The table 2 caption applies here for A-CH$_3$OH ($\nu_t = 1$) and E-CH$_3$OH ($\nu_t = 1$).

Transition	Frequency	E_u	A_{ij}	$\int T_{mb}dV$	V_{lsr}	FWHM
J_k	(MHz)	(K)	(10^{-5} s^{-1})	(K km s^{-1})	(km s^{-1})	(km s^{-1})
A-CH$_3$OH ($\nu_t = 1$)						
$^a7_5$–6_5	337546.048	485.4	8.13	1.047 ± 0.004	-92.8 ± 0.3	9.1 ± 0.5
$^a7_2$–6_2	337625.679	363.5	15.5	10.2 ± 0.9	-90.5 ± 0.3	8 ± 1
$^a7_2$–6_2	337635.655	363.5	15.5	1.2 ± 0.2	-92.6 ± 0.6	9 ± 2
7_1–6_1	337969.414	390.1	16.6	0.39 ± 0.05	-90.8 ± 0.3	5.2 ± 0.7
E-CH$_3$OH ($\nu_t = 1$)						
$^a7_4$–6_4	337581.663	428.2	11.3	–	–	–
$^a7_{-2}$–6_{-2}	337605.255	429.4	15.6	1.513 ± 0.003	-89.8 ± 0.3	11.7 ± 0.5
$^a7_0$–6_0	337643.864	365.4	16.9	1.1 ± 0.8	-90.2 ± 0.2	5.9 ± 0.5
$^b10_{-2}$–11_{-3}	344312.267	491.91	17.7	–	–	–

NOTE—Transitions and quantum numbers from Xu & Lovas (1997) and references therein. Labels indicate the lines partially and totally blended with (a) ^{34}SO 8_8–7_7 (337580 MHz) and (b) SO 8_8–7_7 (344310 MHz).

Table 5. Spectroscopic and observational parameters of the of the $A-^{13}$CH$_3$OH lines analysed in G331. Similarly, the table 2 caption applies here.

Transition	Frequency	E_u	A_{ij}	$\int T_{mb}dV$	V_{lsr}	FWHM	†C/^{13}C
J_k	(MHz)	(K)	(10^{-5} s^{-1})	(K km s^{-1})	(km s^{-1})	(km s^{-1})	
7_0–6_0	330252.798	63.4	15.8	0.60 ± 0.07	-90.7 ± 0.3	5.0 ± 0.6	18.1 ± 0.7
1_1–0_0	350103.118	16.8	32.9	0.69 ± 0.05	-91.2 ± 0.2	4.3 ± 0.3	17.7 ± 0.1

Labels— †Flux ratios derived by considering the integrated fluxes of A-CH$_3$OH (7_0–6_0) and (1_0–0_0) listed in Table 3.

which have exhibited similar frequencies, A_{ij} and E_u values. Then, by selecting the 7_0–6_0 and 1_1–0_0 transitions both of A-CH$_3$OH and A-^{13}CH$_3$OH (Tables 3 and 5), whose A_{ij} values are in agreement almost by a factor 1, we obtained the flux ratios C/^{13}C= 18.1 ± 0.7 and C/^{13}C= 17.7 ± 0.1, respectively. Such flux ratios are similar to the values reported in sources towards the Galactic center, where C/^{13}C= 20 (Wilson & Rood 1994; Requena-Torres et al. 2006). These ratios imply finite values of opacities, therefore in the subsequent sections we will take into account optical depth corrections to estimate the physical conditions derived from the CH$_3$OH and CH$_3$CN emission.

Two lines of E-^{13}CH$_3$OH were also identified, although they exhibited contamination. Close to their rest frequencies, lines of ^{34}SO$_2$ J=8–7 and CH$_3$OCH$_3$ J=16–15 are candidates for blended emission. These contaminants were also detected towards the Hot Molecular Core G34.3+0.15 (MacDonald et al. 1996).

4. PHYSICAL CONDITIONS

### 4.1. *Statistical equilibrium calculations*

In this section we present results based on statistical equilibrium models when considering collisions between the analysed molecules and molecular hydrogen. To estimate the kinetic temperatures and column densities, we ran the RADEX code into CASSIS, whose formalism is analogous to the Large Velocity Gradient approximation (van der Tak et al. 2007). RADEX considers the probability that a photon escape in an isothermal and homogeneous medium without large-scale velocity fields. Collision rate data were collected from the LAMDA database.[7]

Conjointly with RADEX/CASSIS, we used the Markov Chain Monte Carlo (MCMC) method to simulate the observed lines from the resulting best solutions, which are given by the minimal χ^2 value. The MCMC algorithm operates on values chosen randomly within a sample defined by a minimum and maximum limit for an N-dimensional parameter space. This characteristic is the most relevant when calculations require as inputs

[7] Leiden Atomic and Molecular Database LAMDA, http://home.strw.leidenuniv.nl/moldata/

Table 6. Parameters and physical conditions derived from the statistical equilibrium calculations which have yielded hydrogen densities between 0.7 and 1×10^7 cm^{-3}. The number of computed lines and the reduced χ^2 values have also been included.

Parameters	A-CH$_3$CN	E-CH$_3$CN	A-CH$_3$OH	E-CH$_3$OH
Modelled lines	7	13	10	13
χ^2 min	5.69	7.77	6.23	4.42
FWHM (km s^{-1})	5.49 ± 0.01	5.49 ± 0.01	4.9 ± 0.1	4.88 ± 0.01
N (10^{14} cm^{-2})	4.77 ± 0.05	3.69 ± 0.04	85 ± 20	98 ± 0.1
T_k (K)	142.1 ± 0.9	140.5 ± 0.3	64 ± 2	84.8 ± 0.1
θ ($''$)	4.51 ± 0.01	4.53 ± 0.02	5.7 ± 0.3	5.01 ± 0.04
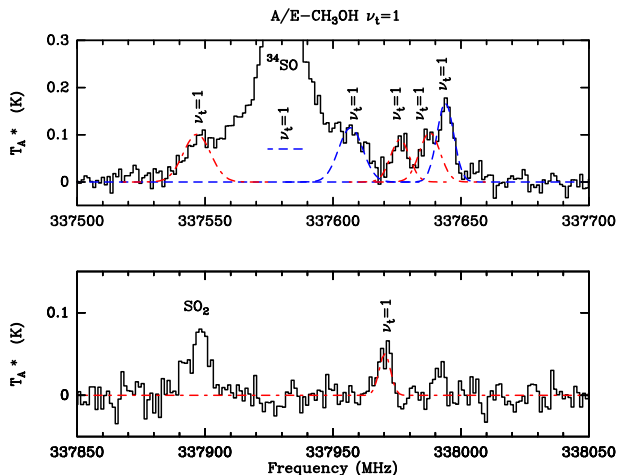
Figure 2. Panels showing the torsional excited lines of A-CH$_3$OH (red dash-dotted line) and E-CH$_3$OH (blue dashed line) against the spectra of G331 (black histogram). In increasing order, the Gaussian fits are centred at the rest frequencies ~ 337546 MHz, 337581 MHz (blended with ^{34}SO), 337605 MHz, 337625 MHz, 337635 MHz, 337643 MHz and 337969 MHz.

several free parameters. In detriment, the quality of the fit is a monotonically increasing function of the number of iterations introduced in the chain, which in turn affects the "computational time" to achieve convergence (e.g. Guan & Krone 2007; Foreman-Mackey et al. 2013; Tahani et al. 2016).

We prepared MCMC routines for each A and E species. The numerical sample explored by the algorithm was delimited by five free parameters: kinetic temperature (T_k), column density (N), source size (θ), FWHM and hydrogen density (n_{H_2}). To guarantee that the code has visited the sample, we tested routines with number of iterations of the order of 10^5. Once the algorithm achieves convergence, the minimal χ^2 is computed printing the statistical results for each parameter. This methodology implied large run-times. As a total, we modelled 7 and 13 lines of A-CH$_3$CN and E-CH$_3$CN, respectively, and 10 and 13 lines of A-CH$_3$OH and E-CH$_3$OH, respectively. The statistical calculations are

summarized in Table 6. Likewise, the best fit model lines are exhibited in Figure 3.

There are two aspects which were common for the models of A/E-CH$_3$OH and A/E-CH$_3$CN. First, we obtained H$_2$ densities in the interval $n_{H_2} = (0.7\text{–}1) \times 10^7$ cm^{-3}, which is in agreement within a factor $\gtrsim 1.5$ with the density derived from the dust continuum (Hervías-Caimapo et al. *submitted*). Also, we intended to differentiate the densities of the ortho-H$_2$ and para-H$_2$ collisional partners (o-H$_2$ and p-H$_2$ respectively). Although studies explain the differences when A and E-species collide with o-H$_2$ and p-H$_2$ (e.g. Rabli & Flower 2010), for our purposes we just conclude that the o-H$_2$/p-H$_2$ ratio varied between ~ 0.6 and 1.0 for the different MCMC computations. That interval is consistent with the ortho-to-para limit of 0.2, when H$_2$ is thermalized at the CO temperature, and ortho-to-para limit of 3 when H$_2$ first forms (Flower & Watt 1984; Lacy et al. 1994).

The second aspect is that the modelled spectral lines yielded source sizes in agreement with a compact emitter region. For CH$_3$CN and CH$_3$OH we found sizes of $\sim 4.5''$ and $\sim 5.3''$, respectively. This result is supported by previous CO (7–6) maps obtained with the Australia Telescope Compact Array (ATCA), for which Bronfman et al. (2008) determined a compact and dense region of $\sim 4.3''$. Merello et al. (2013a,b) mapping the emission traced by SiO (8–7) found a ring-type structure of $\lesssim 5''$.

4.2. *LTE analysis*

Rotational diagrams were constructed to estimate the excitation temperatures (T_{exc}) and column densities (N) of A/E-CH$_3$CN and A/E-CH$_3$OH. Assuming that the emission is optically thin and uniformly fills the antenna beam, T_{exc} and N can be calculated from

$$\ln\left(\frac{N_u}{g_u}\right) = \ln\left(\frac{N}{Z}\right) - \frac{E_u}{kT_{exc}} \qquad (1)$$

where N_u/g_u and E_u are the column density per statistical weight and the energy of the upper level, respectively, and Z is the partition function (Goldsmith & Langer
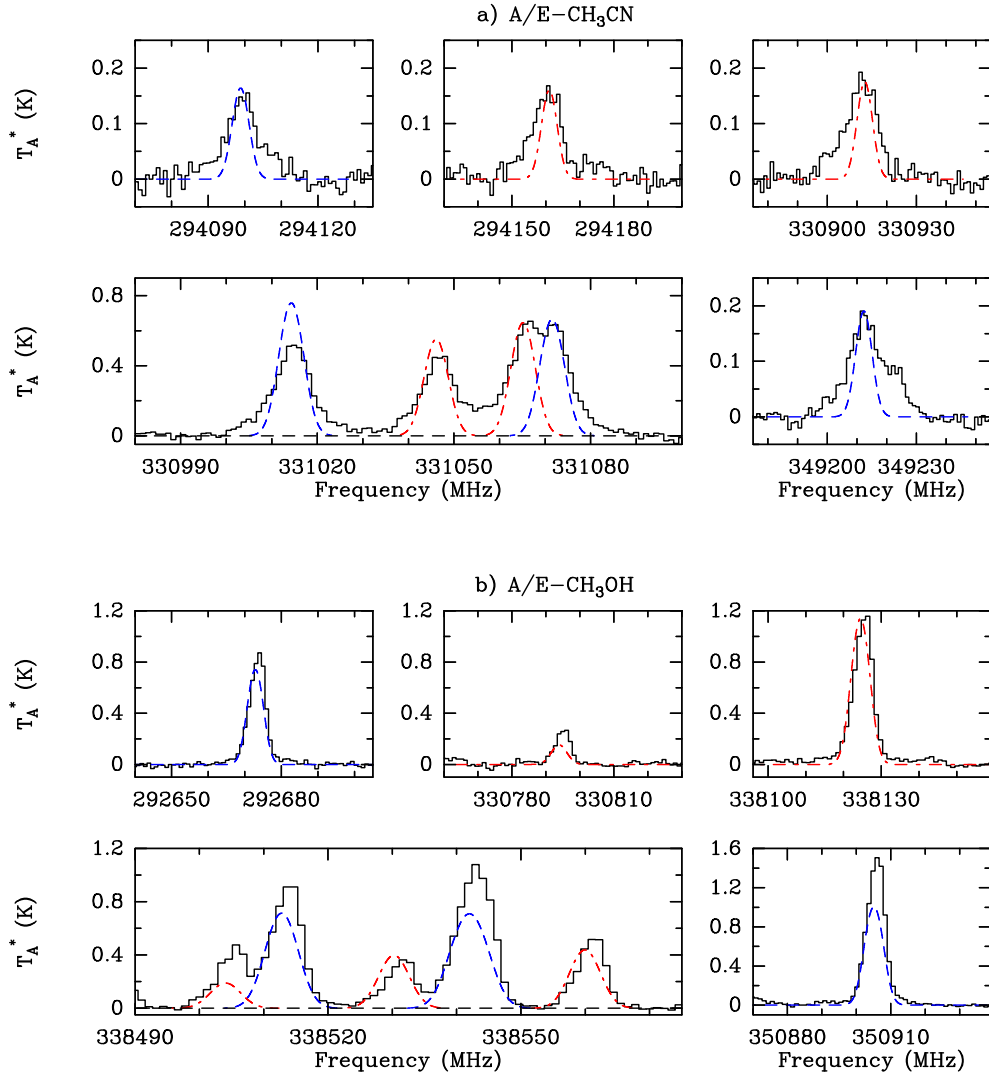
Figure 3. Spectral lines and the best fits assuming non-LTE conditions, plotted as a function of the frequency corrected by the source V_{lsr}, of a) A-CH$_3$CN (blue dashed-line) and E-CH$_3$CN (red dash-dotted-line) and b) A-CH$_3$OH (blue dashed-line) and E-CH$_3$OH (red dash-dotted-line). For A/E-CH$_3$CN, the models yielded a kinetic temperature between $\sim$ (140–142) K and column densities between $\sim$ (3.7–4.8) $\times 10^{14}$ cm^{-2}. For A/E-CH$_3$OH, the models yielded a kinetic temperature between $\sim$ (64–85) K and column densities between $\sim$ (8.5–9.8) $\times 10^{15}$ cm^{-2}.

1999). In local thermodynamic equilibrium (LTE), Equation 1 represents a Boltzmann distribution whose values $\ln N_u/g_u$ vs E_u/k can be fitted using a straight line, whose slope is defined by the term $1/T_{exc}$.

The rotational diagrams were constructed taking a beam dilution factor associated with a point-like emitter region. Therefore, a correction that is provided by the term $\ln(\Delta\Omega_a/\Delta\Omega_s)$ was introduced on the right-hand of Equation 1 (Goldsmith & Langer 1999). This ratio relates the subtended angle of the source with the solid angle of the antenna beam. The beam dilution factor that we introduced is based on the results derived from the RADEX/MCMC calculations. Then, for CH$_3$CN and CH$_3$OH we adopted averaged source sizes of 4.5″ and 5.3″, respectively.

Since the lines observed in this work fell in a broad band, from 290 to 350 GHz, yielding different beamwidths, the adopted sizes have been used in the comparisons between temperatures and column densities for the different lines.

Depending on the density of the region, the K-ladder structures of CH$_3$CN and CH$_3$OH can exhibit an important scattering of $(\ln N_u/g_u, E_u)$-values in their rotational diagrams. More generally, it is expected that the higher is the gas density, the lower is the K-ladder segregation (Olmi et al. 1993; Cesaroni et al. 1997; Goldsmith & Langer 1999; Remijan et al. 2004; Araya et al. 2005; Cuadrado et al. 2017). In order to check the amount of scatter, we compared the rotational

diagrams when they were individually constructed for each J_K level and with those obtained when an unique fit was determined across all the K-levels. As a result, we did not observe considerable discrepancies between the two cases, temperatures and column densities were found within the adopted uncertainty from calibration (§ 2). For instance, in Figure 4 we display the result for E-CH$_3$CN.
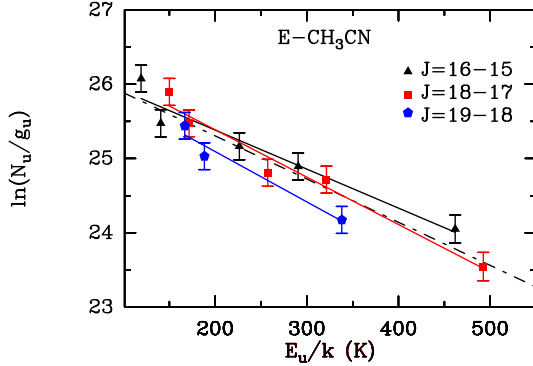
Figure 4. Rotational diagram fits of E-CH$_3$CN across all the K-ladder levels (dashed-dotted line), yielding $N \simeq 7.5 \times 10^{14}$ cm^{-2} and $T_{exc} \simeq 172$ K, and within each K-ladder structure for the transitions J=16–15 (black triangles), J=18–17 (red squares) and J=19–18 (blue pentagons).

OPTICAL DEPTH CORRECTION

The rotational diagrams obtained from the A/E-CH$_3$CN and A/E-CH$_3$OH lines are displayed in Figure 5. They were constructed selecting only the transitions in the ground state and without contaminant emission. So far, the rotational diagrams have been scaled only considering the beam dilution factor. However, they represent a solution under the assumption of emission optically thin, $\tau \ll 1$. In order to revise how different are the LTE solutions from a radiative scenario with finite values of optical depths, we have applied an optical depth correction on the rotational diagrams of A/E-CH$_3$CN and A/E-CH$_3$OH. Expressed mathematically, the correction consisted in including the term $-\ln C_\tau$, with $C_\tau = \tau/1 - \exp^{-\tau}$, on the right side of Equation 1 (Goldsmith & Langer 1999; Gibb et al. 2000; Remijan et al. 2004; Araya et al. 2005). Thus, the ordinates of our rotational diagrams were readjusted considering a term associated with the photon escape probability.

We have performed this adjust based on (1st) the results obtained from the statistical equilibrium calculations. In the case of CH$_3$CN, transitions with K=0,1,2 and 3 were the most affected with $\tau \approx 1$. And, (2nd) considering the flux ratio C/^{13}C$\lesssim$ 20 as we described in section 3.3, which suggests finite optical depths.

In order to perform the optical depth correction, we used CASSIS which executes iterative calculations

of C_τ adjusting the level populations until achieving a consistent solution. With these corrections slight changes are expected in the LTE solutions. For instance, Araya et al. (2005) obtained differences around 10 and 14 % in the temperature and column density of CH$_3$CN when the optical depth correction was applied, respectively.

The A/E-CH$_3$CN rotational diagrams (RDs), with the optical depth correction, are displayed in the upper panels of Figure 5. For A-CH$_3$CN, we obtained $N = (6.4 \pm 2.0) \times 10^{14}$ cm^{-2} and $T_{exc} = 156 \pm 25$ K. For E-CH$_3$CN, we obtained $N = (8.4 \pm 2.0) \times 10^{14}$ cm^{-2} and $T_{exc} = 152 \pm 20$ K. The percentage difference of N and T_{exc}, with respect to the RD without the optical depth correction, are ranged between (5–14) % and (2–12) %, respectively.
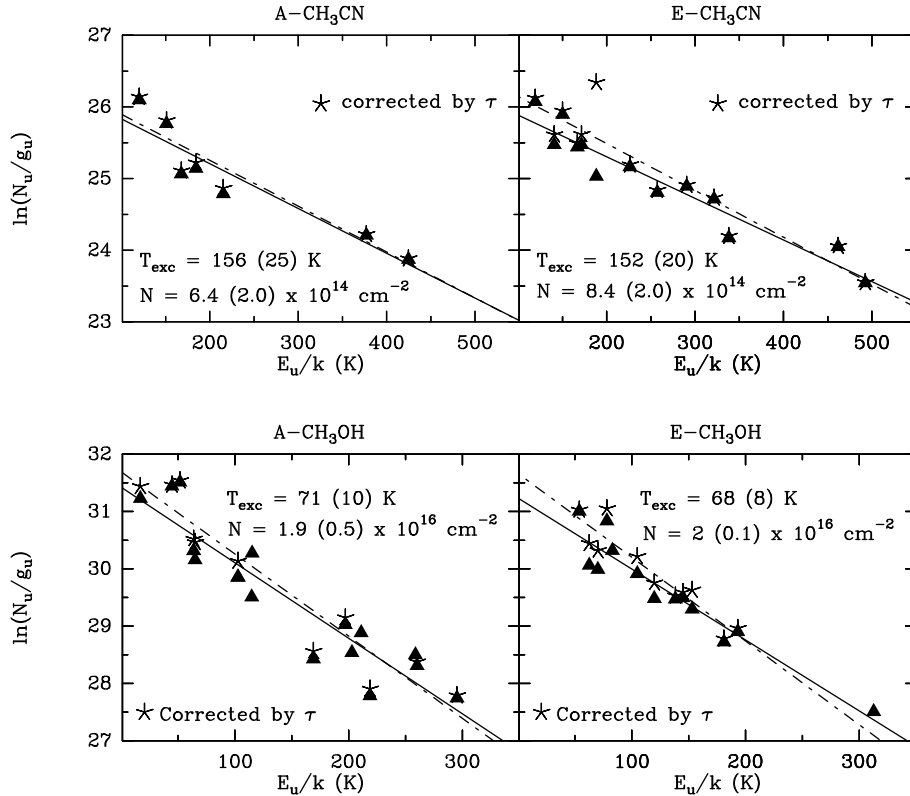
The A/E-CH$_3$OH RDs, with the optical depth correction, are displayed in the lower panels of Figure 5. For A-CH$_3$OH, we obtained $N = (1.9 \pm 0.5) \times 10^{16}$ cm^{-2} and $T_{exc} = 71 \pm 10$ K. For E-CH$_3$OH, we obtained $N = (2.0 \pm 0.1) \times 10^{16}$ cm^{-2} and $T_{exc} = 68 \pm 8$ K. The percentage difference of N and T_{exc}, with respect to the RD without the optical depth correction, are ranged between (10–22) % and (9–17) %, respectively.

We detected two lines of ^{13}CH$_3$OH (Table 5). In the absence of collisional coefficients, those lines were modelled assuming LTE conditions applying the MCMC method leaving various inputs as free parameters: N, T_{exc}, FWHM, and θ. However, we put an upper limit of $N < 5 \times 10^{15}$ cm^{-2}, which was derived from the column density of the main isotopologue and considering the ratio C/^{13}C $\lesssim$ 20. The results were consistent with the physical conditions of the main isotopologue. The best LTE models have been displayed in Figure 6, whose solution (χ^2=2.82) yielded $N = (1.01 \pm 0.06) \times 10^{15}$ cm^{-2} and $T_{exc} = 89.5 \pm 0.4$ K for a modelled source size of 5.7″. Additionally, the resulting FWHM values ($\sim$ 4.4 km s^{-1}) are consistent with the resulting fits reported in Table 5.

5. DISCUSSION

5.1. *Molecular abundances*

CH$_3$OH is more abundant and traces a region about 70 K colder than that traced by CH$_3$CN. From the LTE and non-LTE analysis, we found that the ratio $(A+E)$-CH$_3$OH/$(A+E)$-CH$_3$CN is about 25, indicating almost the same over abundance of A and E-CH$_3$OH over A-CH$_3$CN and E-CH$_3$CN.

ALMA observations of the ion H^{13}CO$^+$ (4–3) probed the existence of a core and various clumpy structures in G331 (Hervías-Caimapo et al. *submitted*). Maps of SiO (8–7) show as well an internal cavity surrounded by molecular emission confined in $\lesssim$ 5″, for which these authors have estimated N(H^{13}CO$^+$)$\approx$(1.5–3) $\times 10^{13}$ cm^{-2} (e.g. Bronfman et al. 2008; Merello et al. 2013a,b).

**Figure 5.** Upper panels. Rotational diagrams of A-CH$_3$CN and E-CH$_3$CN showing the least-square fits with the optical depth correction, represented with the asterisk symbols and dashed-dotted lines, and without the optical depth correction, represented with the filled triangles and solid lines. Bottom panels, the same as above for A-CH$_3$OH and E-CH$_3$OH. Column densities and excitation temperatures correspond to the results when applied the optical depth correction, numbers in parenthesis represent uncertainties on the last digit.

Table 7. Abundances of CH$_3$OH and CH$_3$CN derived from the LTE and non-LTE analysis. We have included the contribution of each spin isomer as a percentage of the total abundance, assumed as the sum $A + E$ of the symmetries.

Method	Hot Component			Cold Component		
	[CH$_3$CN]	[^{13}CH$_3$CN]	$\%_{A-\mathrm{CH_3CN}}$	[CH$_3$OH]	[^{13}CH$_3$OH]	$\%_{A-\mathrm{CH_3OH}}$
	10^{-9}	10^{-9}	$\approx$	10^{-9}	10^{-9}	$\approx$
non-LTE	1.8 ± 0.2	–	56	38 ± 10	–	46
LTE	3.1 ± 0.6	$\lesssim 0.08$	43	81 ± 15	$\lesssim 2.1$	49

The column densities of CH$_3$OH and CH$_3$CN were divided by N(H$_2$) values to obtain their abundances. Following the works cited above, in order to estimate a scaled density of H$_2$ in G331, we applied the ratio H^{13}CO$^+$/H$_2$=3.3 $\times 10^{-11}$ of Orion KL (e.g. Blake et al. 1987) on the H^{13}CO$^+$ column densities derived for G331 (Merello et al. 2013a). As an approximation for the present work, we adopted the H^{13}CO$^+$/H$_2$ ratio of the Orion KL system, since this source is an excellent template for comparative studies on abundances and molecular complexity (e.g. Schilke et al. 2001; Beuther et al. 2005). The total abundances of CH$_3$OH and CH$_3$CN are summarized in Table 7; as a total, we refer to

the $A + E$ contribution from the nuclear spin symmetries (e.g. Fuente et al. 2014). Thus, the CH$_3$CN emission is linked to a hot core with $T_k \approx$141 K and $\theta \approx$4.5″ while CH$_3$OH traces a cold bulk medium with $T_k \approx$74 K and $\theta \approx$5.3″. In the same Table 7, we also included the abundance uncertainties computed from the errors obtained with the radiative models (Bevington & Robinson 2003); although we listed errors of $\lesssim$ 25%, the abundance uncertainties could be of up to 40% including other sources of errors, such as the calibration uncertainty, adopted here as 20%. In Table 7, the abundances of the ^{13}C isotopologues are also listed. Although we obtained an inaccurate result
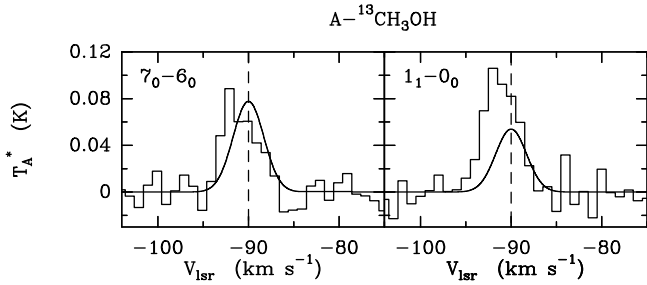
Figure 6. Spectral lines and LTE models of A-$^{13}CH_3OH$ represented by black histograms and Gaussian curves, respectively. Lines 7_0–6_0 and 1_1–0_0 appeared at the rest frequencies 330252.798 MHz and 350103.118 MHz, respectively. The models were derived from a computation whose best solution provided $N = (1.01 \pm 0.06) \times 10^{15}$ cm^{-2} and $T_{exc} = 89.5 \pm 0.4$ K.

based only on two lines of $^{13}CH_3OH$, we found that it could be not only 20 times lower, as resulting from the $^{13}C/C$ flux ratio, but up to 40 times under abundant than CH_3OH, as the LTE analysis suggested (see Figure 6). Thus, we determined $[^{13}CH_3OH] \lesssim 2.1 \times 10^{-9}$. For the undetected $^{13}CH_3CN$, we propose upper limits assuming that the $^{13}CH_3CN/^{13}CH_3OH$ ratio works as what we found for the main isotopologues: $CH_3CN/CH_3OH \approx 1/25$. From that conjecture, we conclude that $[^{13}CH_3CN] \lesssim 8 \times 10^{-11}$.

One of the goals of this work was to separately analyse the emission of the A and E spin nuclear isomers; however, the analysis indicated common physical conditions (N and T) for both spin symmetries meaning that they trace the same reservoir. The opposite case would imply spin conversion processes, induced by molecular interactions on molecular ices or collisions in gas phase, favouring an over-abundance in a given spin symmetry. However, this result would be expected at earlier stages or in younger stellar sources (e.g. Minh et al. 1993; Wirström et al. 2011).

Independently of the employed analysis, we find that both the A and E isomers contribute with approximately half of the total emission of CH_3OH and CH_3CN. The percentage derived from both methods are listed in Table 7, as explained above, assuming a total abundance as $A + E$. As a similar result, MacDonald et al. (1996) determined the ratio $[A$-$CH_3OH]/[E$-$CH_3OH] \approx 0.9$ for the hot molecular core G34.3+0.15. In the envelopes around low-mass protostars, Jørgensen et al. (2005) found ortho-to-para ratios close to unity for CH_3OH. Recently, similar results were reported for the pairs A/E-CH_3CN, A/E-CH_3OH and A/E-CH_3CHO in the Orion Bar photodissociation region (PDR) (Cuadrado et al. 2017).

This tendency is similar to another aspect aimed to examine in this study: whether o- and p-H_2 collisional partners may affect the population of the A and E nuclear spin isomers of CH_3OH and CH_3CN. However,

the MCMC/RADEX computations yielded H_2 ortho-to-para ratios close to unity.

Laboratory studies have offered new measurements about spin conversion, generally assumed as improbable processes. In gas phase, Sun et al. (2015) found that molecular collisions induce the interconversion of spin in molecules of methanol exhibiting a rate that decreases as the pressure increases with the number of collisions. A quantum relaxation mechanism explains the interconversion. In condensed phase, Lee et al. (2006) observed that methanol can suffer a slow conversion from the E to the A symmetry when it is trapped in a solid matrix of p-H_2 prepared at low temperatures (~ 5 K). In theoretical works, Rabli & Flower (2010) studied the implications of methanol colliding with o-H_2 and p-H_2, finding qualitative and quantitative differences for those cases.

As we summarized in Table 4, emission of torsionally excited methanol was also evidenced, however only one line appeared without blended emission: A-CH_3OH (ν_t=1) at $\sim$337969 MHz. In some studies it has been analysed whether excited transitions may be populated at the same LTE conditions of the ground torsional levels (e.g. Lovas et al. 1982; Menten et al. 1986; Sutton et al. 1995; Ren et al. 2011; Sánchez-Monge et al. 2014). We made a minor examination based on the unique line without contamination; however, we found that, to account for the flux, different regimes are needed with $T_{exc} \gtrsim 90$ K. Complementary observations with APEX will be carried out to determine with a better precision the physical conditions of excited methanol in G331.

5.2. *The hot and cold components of G331*

In this study we identified two different components that could candidate G331 as a Hot Molecular Core (HMC). Other characteristics also support this hypothesis. For instance, the source is compact, harbours a massive and energetic molecular outflow, and is embedded in a H II region where masers of OH and CH_3OH reveal a high star formation activity. Besides, the temperatures of the gas components are above and below the limits where evaporation of icy mantles plays an important role; for instance, to explain abundances of Complex Organic Molecules and aspects related to the age of the source. The gas densities also support such classification, since we determined H_2 densities typical of a dense medium $(0.7$–$1) \times 10^7$ cm^{-3}.

N- and O-bearing molecules help to diagnose the presence of different gas components in HMCs (e.g. Beuther & Sridharan 2007; Fontani et al. 2007). In this first work, it is proposed that A/E-CH_3CN and A/E-CH_3OH trace a hot ($T_k \simeq 141$ K) and cold ($T_k \simeq 75$ K) component with sizes around 4.5″ and 5.3″, respectively. Such results are in agreement with ALMA obser-
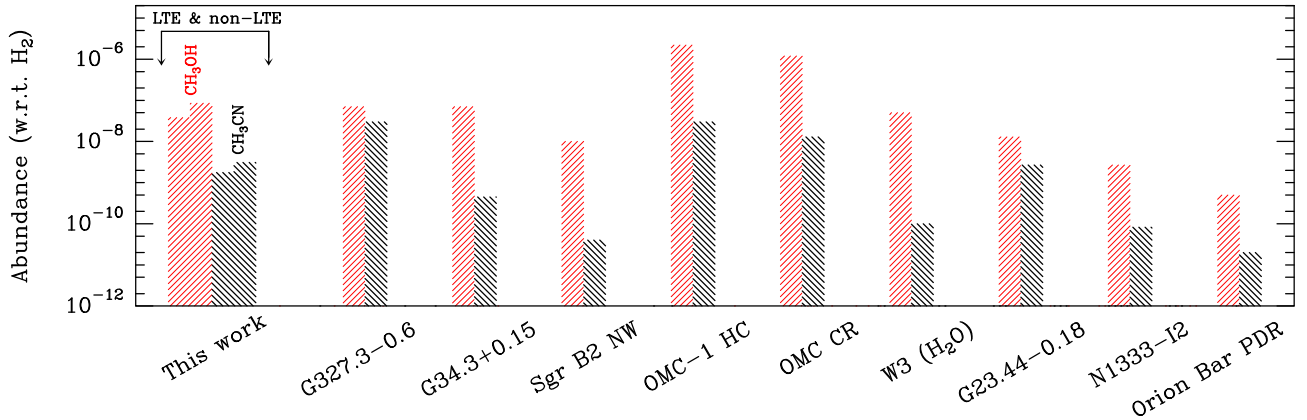
Figure 7. Comparison of the abundances of CH$_3$OH (red) and CH$_3$CN (black) in hot molecular cores, clouds, PDR regions. Values were collected from Sutton et al. (1995); MacDonald et al. (1996); Helmich & van Dishoeck (1997); Gibb et al. (2000); Nummelin et al. (2000); Ren et al. (2011); Crockett et al. (2014) and Cuadrado et al. (2017).

vations of CO (7–6), SiO (8–7) and H^{13}CO$^+$ (4–3). The emission of these species was found to be compacted in $\sim 5''$ (Bronfman et al. 2008; Merello et al. 2013a; Hervías et al. 2015).

In Figure 7, we compare the abundances derived in this work with other sources. Our results are similar with the abundances reported in G34.3+0.15. More generally, our results suggest different abundances, physical components and a chemical differentiation for CH$_3$OH and CH$_3$CN in G331. The high sensitivity and spectral resolution of our single-dish spectra have been useful to realise subtle differences in the line profiles of CH$_3$OH and CH$_3$CN, inspected via the V_{lsr} and FWHM parameters listed in Tables 2 and 3. In agreement with the radiative models, these spectral signatures reveal clues on the origin and size of the emitter regions. In spite of that, and as a perspective, further observations at higher spatial resolution are needed to study the spatial distribution of different tracers in G331. As well, these observations may reveal density gradients towards the core and the outflow, allowing more accurate determinations of molecular abundances.

The fact of CH$_3$OH being more abundant than CH$_3$CN is in agreement with the chemistry that has been modelled in HMCs, where these molecules are usually referred as parent and daughter species, respectively, since CH$_3$OH is expected to be formed at early stages in grain surfaces, via successive hydrogenation of CO, while CH$_3$CN appears later via reaction between HCN and CH$_3^+$ (Millar et al. 1997; Nomura & Millar 2004; Guzmán et al. 2013; Loison et al. 2014). Other alternatives to produce methanol are CH$_3^+$ + OH → CH$_3$OH and CH$_2$ + H$_2$O → CH$_3$OH. They can occur when frozen mixtures of CH$_4$ and H$_2$O are bombarded with electrons (Hiraoka et al. 2006). In addition, we have found that the physical conditions traced by those molecules might explain the regimes where pre-biotic and complex organic molecules have been detected, such

as CH$_3$OCH$_3$, CH$_3$CHO, NH$_2$CHO and the C$_2$H$_4$O$_2$ isomers.

Nomura & Millar (2004) performed time-dependent chemical models considering observational aspects of the hot molecular core G34.3+0.15; for instance, that CH$_3$CN is associated to an inner and hot core region while CH$_3$OH traces the gas present in clumps (e.g. Hatchell et al. 1998; Millar & Hatchell 1998; van der Tak et al. 2000). Comparing our column densities with the temporal values calculated by these authors, an age of 10^4 yr may represent the epoch for G331, when substantial quantities of daughters molecules (e.g. CH$_3$CN) are produced without substantially decimate their parents (e.g. CH$_3$OH). Preliminary results derived by us, obtained with the gas-grain chemical code Nautilus (Ruaud et al. 2016),[8] shows a CH$_3$OH/CH$_3$CN ratio similar to those derived from the observations. However, these results will be presented in a subsequent work depicting the chemistry of O-bearing molecules detected in the source.

6. CONCLUSIONS AND PERSPECTIVES

As an active interstellar laboratory, the G331.512-0.103 system exhibits a rich chemistry in organic and pre-biotic molecules. In this first article, we analysed around 70 lines of A/E-CH$_3$OH and A/E-CH$_3$CN towards the central region, abbreviated here as G331. Torsionally excited transitions of methanol were evidenced. Without contaminant emission, we identified the CH$_3$OH (ν_t=1) 7_1–6_1 transition. Likewise, two lines corresponding to ^{13}CH$_3$OH were detected at 330252.798 MHz and 350103.118 MHz.

The analyses were performed including collisions with H$_2$ and typical radiative processes under LTE conditions, namely: rotational diagrams. Both analyses coincide in that CH$_3$OH traces a cold component while

---

[8] http://kida.obs.u-bordeaux1.fr/networks.html

CH$_3$CN traces a hotter core with kinetic temperatures of $\sim$ 74 K and 141 K, respectively. Likewise, the best-fits indicated emitter regions of around $4.5''$ and $5.3''$ for these tracers, respectively, with gas density $n(\mathrm{H}_2)=(0.7-1) \times 10^7$ cm^{-3}.

We treated independently each one of the nuclear spin isomers of CH$_3$OH and CH$_3$CN, and determined the ratio $(A + E)$-CH$_3$OH/$(A + E)$-CH$_3$CN$\simeq 25$. The temperatures and densities of each A and E pair suggest that they trace a same bulk and are equally populated at each local temperature. Considering that, we estimated the CH$_3$OH and CH$_3$CN abundances from the total contribution $A + E$. Under the LTE formalism, we estimated that [CH$_3$OH]$\approx 8.1 \times 10^{-8}$, [CH$_3$CN]$\approx 3.1 \times 10^{-9}$, and the upper limits [^{13}CH$_3$OH]$\approx 2.1 \times 10^{-9}$ and [^{13}CH$_3$CN]$\approx 8 \times 10^{-11}$.

Under the perspective of hot molecular cores, the CH$_3$OH/CH$_3$CN ratio could be associated with and epoch between (10^4-10^5) yr, when daughter molecules like CH$_3$CN start to be produced from parent molecules, such as CH$_3$OH.

Facility: Atacama Pathfinder EXperiment, APEX telescope

Software: CASSIS (http://cassis.irap.omp.eu/), GILDAS (https://www.iram.fr/IRAMFR/GILDAS/), RADEX (http://doi.org/10.1051/0004-6361:20066820) NAUTILUS (https://doi.org/10.1093/mnras/stw887)

REFERENCES

Andersson, M., Askne, J., & Hjalmarson, A. 1984, A&A, 136, 243

Araya, E., Hofner, P., Kurtz, S., Bronfman, L., & DeDeo, S. 2005, ApJS, 157, 279

Beuther, H., & Sridharan, T. K. 2007, ApJ, 668, 348

Beuther, H., Zhang, Q., Greenhill, L. J., et al. 2005, ApJ, 632, 355

Bevington, P. R., & Robinson, D. K. 2003, Data reduction and error analysis for the physical sciences, 3rd ed., by Philip R. Bevington, and Keith D. Robinson. Boston, MA: McGraw-Hill, ISBN 0-07-247227-8, 2003.

Blake, G. A., Sutton, E. C., Masson, C. R., & Phillips, T. G. 1987, ApJ, 315, 621

Boucher, D., Burie, J., Bauer, A., Dubrulle, A., & Demaison, J. 1980, Journal of Physical and Chemical Reference Data, 9, 659

Bronfman, L., Garay, G., Merello, M., et al. 2008, ApJ, 672, 391

Caswell, J. L. 1998, MNRAS, 297, 215

Cesaroni, R., Felli, M., Testi, L., Walmsley, C. M., & Olmi, L. 1997, A&A, 325, 725

Crockett, N. R., Bergin, E. A., Neill, J. L., et al. 2014, ApJ, 787, 112

Cuadrado, S., Goicoechea, J. R., Cernicharo, J., et al. 2017, ArXiv e-prints, arXiv:1705.06612

Cummins, S. E., Green, S., Thaddeus, P., & Linke, R. A. 1983, ApJ, 266, 331

Flower, D. R., & Watt, G. D. 1984, MNRAS, 209, 25

Fontani, F., Pascucci, I., Caselli, P., et al. 2007, A&A, 470, 639

Foreman-Mackey, D., Hogg, D. W., Lang, D., & Goodman, J. 2013, PASP, 125, 306

Fuente, A., Cernicharo, J., Caselli, P., et al. 2014, A&A, 568, A65

Giannetti, A., Leurini, S., Wyrowski, F., et al. 2017, A&A, 603, A33

Gibb, E., Nummelin, A., Irvine, W. M., Whittet, D. C. B., & Bergman, P. 2000, ApJ, 545, 309

Goldsmith, P. F., & Langer, W. D. 1999, ApJ, 517, 209

Guan, Y., & Krone, S. M. 2007, ArXiv Mathematics e-prints, math/0703021

Güsten, R., Nyman, L. Å., Schilke, P., et al. 2006, A&A, 454, L13

Guzmán, V. V., Goicoechea, J. R., Pety, J., et al. 2013, A&A, 560, A73

Hatchell, J., Thompson, M. A., Millar, T. J., & MacDonald, G. H. 1998, A&A, 338, 713

Helmich, F. P., & van Dishoeck, E. F. 1997, A&AS, 124, doi:10.1051/aas:1997357

Hervías, C., Bronfman, L., Merello, M., et al. 2015, in Astronomical Society of the Pacific Conference Series, Vol. 499, Revolution in Astronomy with ALMA: The Third Year, ed. D. Iono, K. Tatematsu, A. Wootten, & L. Testi, 229

Hiraoka, K., Mochizuki, N., & Wada, A. 2006, in American Institute of Physics Conference Series, Vol. 855, Astrochemistry - From Laboratory Studies to Astronomical Observations, ed. R. I. Kaiser, P. Bernath, Y. Osamura, S. Petrie, & A. M. Mebel, 86–99

Hugo, E., Asvany, O., & Schlemmer, S. 2009, JChPh, 130, 164302

Jewell, P. R., Hollis, J. M., Lovas, F. J., & Snyder, L. E. 1989, ApJS, 70, 833

Jørgensen, J. K., Hogerheijde, M. R., Blake, G. A., et al. 2004, A&A, 415, 1021

Jørgensen, J. K., Schöier, F. L., & van Dishoeck, E. F. 2005, A&A, 437, 501

Lacy, J. H., Knacke, R., Geballe, T. R., & Tokunaga, A. T. 1994, ApJL, 428, L69

Lee, Y.-P., Wu, Y.-J., Lees, R. M., Xu, L.-H., & Hougen, J. T. 2006, Science, 311, 365

Lees, R. M., & Baker, J. G. 1968, JChPh, 48, 5299

Loison, J.-C., Wakelam, V., & Hickson, K. M. 2014, MNRAS, 443, 398

Lovas, F. J., Bass, J. E., Dragoset, R. A., & Olsen, K. J. 2009, National Institute of Standards and Technology, Gaithersburg, MD.

Lovas, F. J., Suenram, R. D., Snyder, L. E., Hollis, J. M., & Lees, R. M. 1982, ApJ, 253, 149

MacDonald, G. H., Gibb, A. G., Habing, R. J., & Millar, T. J. 1996, A&AS, 119, 333

Menten, K. M., Walmsley, C. M., Henkel, C., et al. 1986, A&A, 169, 271

Merello, M., Bronfman, L., Garay, G., et al. 2013a, ApJL, 774, L7

—. 2013b, ApJ, 774, 38

Millar, T. J., & Hatchell, J. 1998, Faraday Discussions, 109, 15

Millar, T. J., MacDonald, G. H., & Gibb, A. G. 1997, A&A, 325, 1163

Minh, Y. C., Irvine, W. M., Ohishi, M., et al. 1993, A&A, 267, 229

Müller, H. S. P., Schlöder, F., Stutzki, J., & Winnewisser, G. 2005, Journal of Molecular Structure, 742, 215

Nomura, H., & Millar, T. J. 2004, A&A, 414, 409

Nummelin, A., Bergman, P., Hjalmarson, Å., et al. 2000, ApJS, 128, 213

Nyman, L.-Å., Lerner, M., Nielbock, M., et al. 2001, The Messenger, 106, 40

Olmi, L., Cesaroni, R., & Walmsley, C. M. 1993, A&A, 276, 489

Pickett, H. M., Poynter, R. L., Cohen, E. A., et al. 1998, JQSRT, 60, 883

Rabli, D., & Flower, D. R. 2010, MNRAS, 406, 95

Remijan, A., Sutton, E. C., Snyder, L. E., et al. 2004, ApJ, 606, 917

Ren, J. Z., Liu, T., Wu, Y., & Li, L. 2011, MNRAS, 415, L49

Requena-Torres, M. A., Martín-Pintado, J., Rodríguez-Franco, A., et al. 2006, A&A, 455, 971

Risacher, C., Vassilev, V., Monje, R., et al. 2006, A&A, 454, L17

Ruaud, M., Wakelam, V., & Hersant, F. 2016, MNRAS, 459, 3756

Sánchez-Monge, Á., Beltrán, M. T., Cesaroni, R., et al. 2014, A&A, 569, A11

Sandell, G., Knee, L. B. G., Aspin, C., Robson, I. E., & Russell, A. P. G. 1994, A&A, 285

Schilke, P., Benford, D. J., Hunter, T. R., Lis, D. C., & Phillips, T. G. 2001, ApJS, 132, 281

Solomon, P. M., Jefferts, K. B., Penzias, A. A., & Wilson, R. W. 1971, ApJL, 168, L107

Sun, Z.-D., Ge, M., & Zheng, Y. 2015, Nature, 6877, 1

Sutton, E. C., Jaminet, P. A., Danchi, W. C., & Blake, G. A. 1991, ApJS, 77, 255

Sutton, E. C., Peng, R., Danchi, W. C., et al. 1995, ApJS, 97, 455

Tahani, K., Plume, R., Bergin, E. A., et al. 2016, ApJ, 832, 12

van der Tak, F. F. S., Black, J. H., Schöier, F. L., Jansen, D. J., & van Dishoeck, E. F. 2007, A&A, 468, 627

van der Tak, F. F. S., van Dishoeck, E. F., & Caselli, P. 2000, A&A, 361, 327

Willacy, K., Williams, D. A., & Minh, Y. C. 1993, MNRAS, 263, L40

Wilson, T. L., & Rood, R. 1994, ARA&A, 32, 191

Wirström, E. S., Geppert, W. D., Hjalmarson, Å., et al. 2011, A&A, 533, A24

Wyrowski, F., Schilke, P., Walmsley, C. M., & Menten, K. M. 1999, ApJL, 514, L43

Xu, L.-H., & Lovas, F. J. 1997, Journal of Physical and Chemical Reference Data, 26, 17